## REPORTS

# No Evidence of a Circumsolar Dust Ring from Infrared Observations of the 1991 Solar Eclipse

P. Lamy, J. R. Kuhn, H. Lin, S. Koutchmy, R. N. Smartt

**During the past 25 years there have been many attempts to detect a possible dust ring around the sun, with contradictory results. Before the 1991 eclipse, infrared eclipse experiments used single-element detectors to scan the corona along the ecliptic for excess surface brightness peaks. The availability of relatively large-format infrared array detectors now provides a considerable observational advantage: two-dimensional mapping of the brightness and polarization of the corona with high photometric precision. The 1991 eclipse path included the high-altitude Mauna Kea Observatory, a further advantage to measure the corona out to large angular distances from the sun. Results are reported from an experiment conducted on Mauna Kea with a HgCdTe-array detector sensitive to wavelengths between 1 and 2.5 micrometers, using broad-band J, H, and K filters. Although the sky conditions were not ideal, the H- and K-band surface brightnesses clearly show the inhomogeneous structure in the K-corona and the elliptical flattening of the F-corona, but no evidence of a circumsolar, local dust component out to 15 solar radii.**

In the classical views of Allen (*1*) and Van de Hulst (*2*), the Fraunhofer or F-corona results from sunlight scattered by interplanetary dust particles (IDP) located between Earth and the sun. The bulk of these particles being far from the sun, the sunlight is, strictly speaking, diffracted. This results in a very low, nearly zero, polarization, a property extensively used to separate the F-corona from the highly polarized K-corona. Color observations have revealed a strong reddening that is interpreted as an additional contribution to the observed corona; this reddening is due to thermal emission of hot dust grains near the sun (*3, 4*), a first hint of the value of probing the circumsolar region in the infrared (IR). Belton (*5*) suggested that the dynamical evolution of the IDP could lead to regions of density enhancement near the sun. In simple terms, the dust grains orbiting the sun are subjected to dissipative forces, mainly the Poynting-Robertson effect, which produce an inward spiraling of the IDP toward the sun. When the grains reach some critical distance, which depends on their composition, they start to sublimate. As their orbital radius decreases, the relative importance of the radiation pressure force compared to the solar gravitational attraction increases, and the inward spiraling is slowed down, stopped, or possibly reversed. Some grains may be blown away on hyperbolic orbits, but most "oscillate" in narrow circumsolar regions until they disappear. Detailed numerical integrations (*6, 7*) have predicted typical radial distances for zones corresponding to IDP concentrations. With temperatures of 1000 to 1300 K, the thermal emission of silicate grains exhibits a broad maximum at wavelengths of 2 to 3 μm, with an additional peak at 10 μm.

Attempts to observe the corona in this spectral range date back to the times of Lord Kelvin (*8*) and T. A. Edison (*9*). Accurate measurements of possible coronal structures are fundamentally difficult because the average brightness of the corona decreases by about four orders of magnitude from the solar limb to 6 solar radii ($R_\odot$). Hence, the required photometric precision demands high linearity in the detection system and accurate calibration. Relevant observations have been reviewed by Koutchmy and Lamy (*10*). In short, there have been positive results (peaks detected) as well as negative results. The positive ones do not agree completely either in the location of the peaks or in their brightness profiles. One example comes from the balloon experiment of Mizutani *et al.* (*11*) flown during the 1983 eclipse: a peak located at 3.8 $R_\odot$ is well detected at 1.65 μm but is absent at other wavelengths.

The contribution of local, "coronal" dust to the F-corona also has direct implications for the polarization: from Earth, the IDP close to the sun scatters light at nearly 90°, so a local Fraunhofer component should show a large polarization. Thus, the ideal instrument with which to detect the elusive local IDP should be capable of mapping the IR brightness, color, and polarization of the corona with high sensitivity over a large dynamic range.

The detector is a 128 by 128 pixel HgCdTe-array device, produced by Rockwell International (part TCM-1000C). Each pixel has a large photoelectron-well capacity ($3 \times 10^7$) with a read noise of about 2000 electrons. Our detector has an average quantum efficiency of about 70% for light of wavelengths 1 to 2.5 μm. The array operates at liquid nitrogen temperature, behind cold filters, polarizers, and a 110-mm *f.l.*, *f*/2 (stopped down to *f*/4 during the experiment) doublet objective mounted in the Dewar. Figure 1 is a schematic diagram of the eclipse experiment. Standard (Barr Associates, Inc.) IR H-band ($\bar\lambda$ = 1.6 μm) and K-band ($\bar\lambda$ = 2.28 μm) filters and three J-band ($\bar\lambda$ = 1.25 μm) filters with type HR (Polaroid, Inc.) sheet polarizers are mounted on the cooled wheel assembly. The filter wheel is controlled by the experiment computer via an electric motor outside the Dewar. Because of the large wavelength range of the observations, we used an internally mounted stepper motor to make focus adjustments. The final image scale ranged between 0.094 and 0.098 $R_\odot$/pixel, covering a field of ~3.2°, or ± 6 $R_\odot$. The detector system is described more fully elsewhere (*12*).

To avoid scattered light in the optics, for example, due to multiple reflections from the lens at a level $\sim 10^{-3}$ of the surface brightness at the center of the field, we externally occulted the bright inner corona with a mask approximately 1.4 m in front of the focal plane. The mask supported a removable occulting disk 3 cm in radius that was positioned in a 6-cm-radius opening. With the central disk removed, the telescope could be tilted away from the sun to view the outer corona (so that the bright inner corona did not illuminate the telescope optics).

The Dewar and occulter assembly were mounted on a simple equatorial suntracker. During the eclipse we manually shifted the telescope to the west to see the outer corona. Because the moon's limb was not in the field of the IR array during the offset observations, a camcorder with a large field of view was mounted on the tracker and was used to spatially register data frames.

The observations were made at the summit of Mauna Kea (Big Island, Hawaii) at an altitude of 4200 m (latitude, +19°49′6; longitude, −155°28′3). The parameters of the eclipse, including the topocentric correction, were as follows: date: 11 July 1991; local time (universal time − 10 hours): 7h 30m 14.7s (maximum eclipse); duration of totality: 4m 12.0s; zenith distance of the sun: 69°; radius of the moon: 1019.5 arc sec; radius of the sun: 944 arc sec; magnitude of the eclipse: 1.033.

The weather conditions during the eclipse were far from ideal. Ten days before the eclipse the cloud of volcanic dust originating from the eruption of Mount Pinatubo (Philippine Islands) arrived above the Hawaiian Islands, creating high-altitude cirrus

P. Lamy, Laboratoire d'Astronomie Spatiale, Marseille, France.
J. R. Kuhn and H. Lin, Department of Physics and Astronomy, Michigan State University, East Lansing, MI 48824.
S. Koutchmy, Institut d'Astrophysique, CNRS, Paris, France.
R. N. Smartt, National Solar Observatory/Sacramento Peak, Sunspot, NM 88349.

clouds. The night before the eclipse, a capricious intertropical front produced a thick layer of cloud below the summit and hazy cloudiness above it. The result was a bright sky background with excessive scattering.

The IR array images were calibrated as for optical charge-coupled device data. Flat fields were obtained separately for each of the polarization angles, occulter positions, and wavelengths from blank-sky observations. We calibrated field-flattened flux data, using observations of Vega and Altair obtained on the night of 9 July. Unfortunately, the sky conditions during the eclipse were far from photometric and we estimate that our overall flux calibration may be in error by as much as 60%.

The combined scattering function of the sky and optics can be estimated by taking the difference between two eclipse images obtained in rapid succession near second or third contact (*13*). Figure 2 plots our estimate of the scattered-light coronal aureole in the H- and K-bands obtained in this way, as well as the calibrated, circularly averaged, H and K surface brightness. The aureole declines more rapidly in the longer wavelength band, that is, the scattered light becomes bluer farther from the limb. This may explain the apparent blue anomaly that has been observed in the past (*10*), although the color determination is quite sensitive to the subtraction of atmospheric scattered light.

We combined the centered short- and long-exposure K-band data with the offset frames in order to construct a composite image that shows the coronal surface brightness from the limb of the moon out to about 14 $R_\odot$. The noncircular part of the resulting image is shown in Fig. 3 and is based on a logarithmic intensity scale. The mean K-band brightness and the visible-band K- and F-coronal results of Koutchmy and Lamy (*10*) are plotted in Fig. 4. Several points should be noted: (i) neither the visible nor the IR data have been rescaled before plotting these curves; (ii) both results show a "break" in the surface brightness near $2.5 R_\odot$, beyond which the F-corona dominates the K-corona surface brightness; and (iii) there is an apparent scale difference between the visible and the IR data, in the sense that the IR data are everywhere brighter than the visible-band predictions. However, the Koutchmy-Lamy results were obtained for a K-corona of minimum type, whereas the 1991 corona was close to the maximum of a very active solar cycle. Furthermore, their F-corona model pertains to the visible (0.5 μm) and does not include a reddening such as observed by Blackwell (*3*). Given our calibration uncertainty, it is clear that the IR data are consistent with the visible wavelength coronal model and show no anomalous surface brightness bumps out to at least 8 $R_\odot$.

We also searched for anomalous polarization "rings" as evidence of a local F-corona. Figure 5 shows the J-band polarization direction in those pixels with polarization greater than 0.1. The circular average polarization shows a rapid drop from 0.3 to 0.05 near 2 $R_\odot$, which is consistent with the inflection in the K-band light evident in Fig. 4, the "boundary" of the K-corona. Polarization images show that the circular mean polarization within 3 $R_\odot$ is dominated by the polarization of the complex geometry of the streamers.

Although the sky conditions were far from ideal because of the volcanic dust, our observations clearly show advantages of imaging in the IR in comparison with imaging in the visible. The corona is well detected out to 15 $R_\odot$. With a perfect sky at an altitude of 4200 m, it is possible, in principle, to measure the corona out to ~30 $R_\odot$. Nevertheless, even in the K-band, the inner corona is dominated by the K-corona component. Its radial extension strongly depends on the solar activity (*14*) and on the plasma structures. Large streamers may be followed out to 10 $R_\odot$ in our K-band images, consistent with an eclipse close to the maximum of the activity cycle. The role of the K-corona has probably not been fully taken into account in past IR observations in which single, diametrical scans were "blindly" obtained. Asymmetries reported, for instance, by Lamy and Koutchmy (*15*) and Mizutani *et al.* (*11*) were likely due to structures in the coronal plasma. With the advance of two-dimen-

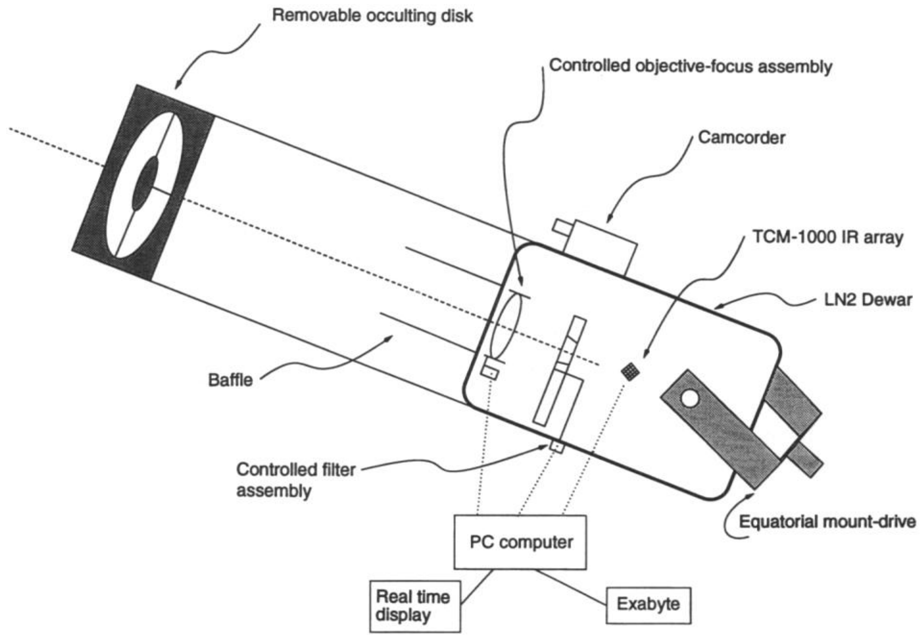


**Fig. 1.** A schematic diagram of the principal components of the eclipse experiment. The principal optical components of the telescope were controlled by a computer, which was required to complete the complicated observing sequence during the 4 min of totality.

**Fig. 2.** The calibrated H- and K-band surface brightnesses. The scattered light contribution is also plotted here. The brightness measurements were obtained from a circular average of the two-dimensional data array.

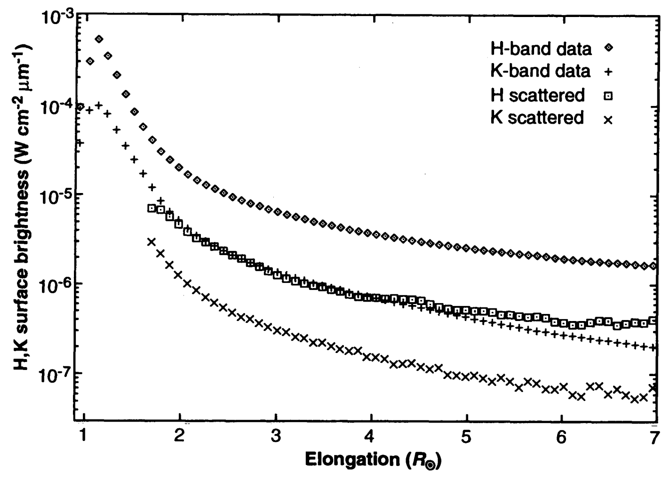

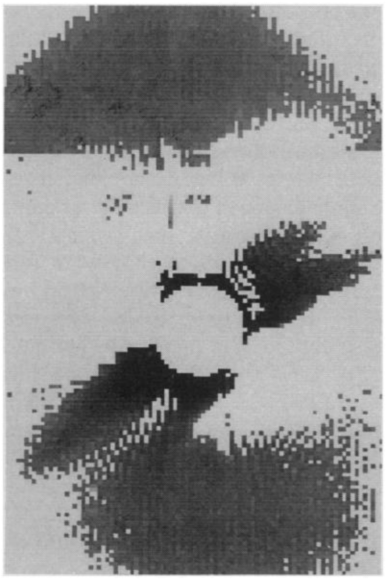

**Fig. 3.** The offset K-band data have been combined with the centered data to construct this composite image. A sun-centered circular average of the data has been subtracted to yield the residual surface brightness displayed here. The streamers near the center of the image shine from reflected IR light due to hot electrons in the sun's K-corona. The patches of light farther from the sun glow from photospheric sunlight reflected by interplanetary dust which is approximately ten thousand times fainter than the K-corona light ("zodaical light").

**Fig. 4.** The mean K-band brightness and the Koutchmy-Lamy K- and F-coronal model (*10*). The curves are obtained from sun-centered circular averages of the two-dimensional data array.

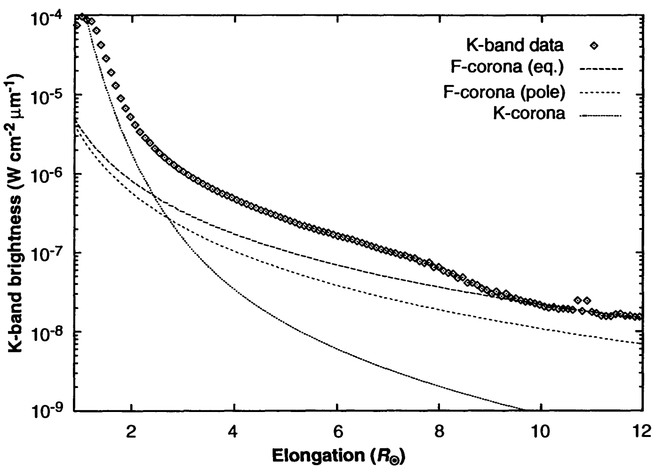


**Fig. 5.** The direction and magnitude of the J-band polarization. The length of each line segment is proportional to the polarization fraction, and its direction shows the polarization plane.

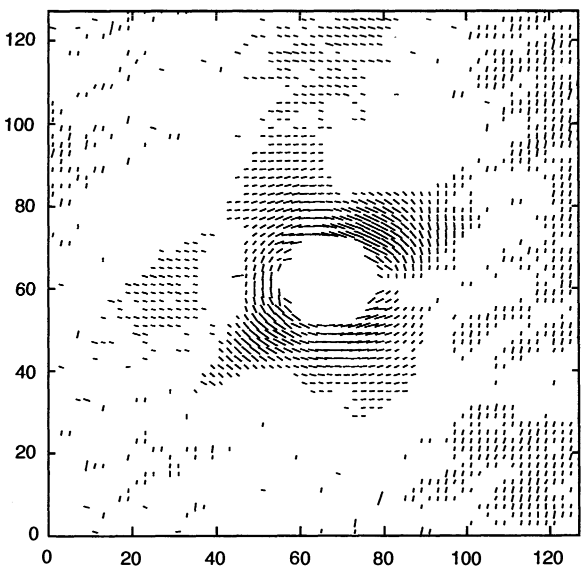


sional images that conspicuously reveal the IR K-corona structures, observational uncertainties are substantially reduced.

In view of the past contradictory results, the absence of surface brightness "peaks" is not surprising. Real peaks such as those detected by Peterson (*16–18*) and MacQueen (*19*) would require a narrow ring (or cocoon) of dust with a large enhanced spatial density above the background dust cloud. Such an ad hoc model was worked out by Mukai and Yamamoto (*20*), combining graphite and silicate grains with excess concentrations above the local density by factors of respectively, 10 and 5, concentrated in very narrow rings. Apart from the fact that there is no dynamical justification for these enormous concentrations, the model meets serious difficulties: (i) it produces a peak in the visible ($\lambda$ = 0.57 μm) that is not observed; (ii) it relies heavily on the presence of graphite, whose presence in the solar system is highly questionable; in comets and meteorites the bulk of the carbon is found in carbonaceous compounds that are thermally dissociated at temperatures of 500 to 600 K, that is, at heliocentric distances $R > 30\ R_\odot$ (*21*).

Numerical calculations imply that the elliptical orbits of circumsolar dust grains cover a region much broader than a few tenths of a solar radius reported by Peterson (*17*). A further broadening results from the different composition of the grains: different properties of light absorption lead to variations in the temperature distribution and in the heliocentric distances where the sublimation is efficient. In fact, the models predict broad, extended reinforcements rather than peaks. The solar wind and the interplanetary magnetic field give rise to a gas-kinetic drag and electromagnetic force drags (*5*), respectively, on the charged circumsolar grains and may further spread their orbits.

Another difficulty was encountered by Peterson (*18*) with his observation of the emission features at 4 $R_\odot$: combining the brightness values at 0.84, 1.57, and 2.23 μm, he obtained a blackbody temperature of 2160 ± 200 K, considerably higher than the temperatures of 1000 to 1300 K predicted by the models. Any claim of refractory, exotic material would face the barrier of element abundances in the solar system. Here again the result points to a problem with the observations.

Our IR brightness and polarization measurements support the classical interpretation of the F-corona: a significant local dust component and its large-angle scattered polarized light component are excluded. This is consistent with the in-depth analysis of Lamy and Perrin (*22*), who found that the interplanetary dust is not highly concentrated around the sun. In situ measurements made with impact detectors aboard the two Helios probes, which reached a heliocentric distance of 60 $R_\odot$, have also shown that the spatial IDP density gradually levels off inside ~100 $R_\odot$.

Our two-dimensional IR observations have shown unambiguously that a prominent circumsolar dust ring did not exist at the time of the 11 July 1991 solar eclipse. Consistent with these results, a second recent IR eclipse experiment also found no evidence of surface brightness enhancements (*23*). Our results imply that the dynamics of the IDP are more complicated than the simple gravitational-radiation drag calculations suggest. All the evidence taken together leads us to conclude that earlier reported detections of such dust rings are unlikely to be due to "local" coronal dust rings.


### REFERENCES AND NOTES

1. C. W. Allen, *Mon. Not. R. Astron. Soc.* **106**, 137 (1946).
2. H. C. Van de Hulst, *Astrophys. J.* **105**, 471 (1947).
3. D. E. Blackwell, *Mon. Not. R. Astron. Soc.* **112**, 652 (1952).
4. A. W. Peterson, *Astrophys. J.* **138**, 1218 (1963).
5. M. J. S. Belton, *Science* **151**, 35 (1966).
6. P. L. Lamy, *Astron. Astrophys.* **33**, 191 (1974).
7. T. Mukai, T. Yamamoto, H. Hasegawa, A. Fujiwara, C. Koike, *Publ. Astron. Soc. Jpn.* **26**, 445 (1974).
8. N. M. Kelvin, *Mon. Not. R. Astron. Soc.* **20**, 317 (1860).
9. T. A. Edison, *Am. J. Sci.* **117**, 52 (1879).
10. S. Koutchmy and P. L. Lamy, in *Properties and Interactions of Interplanetary Dust*, R. H. Giese and P. Lamy, Eds. (Reidel, Dordrecht, Netherlands, 1985), p. 63.
11. M. Mizutani *et al.*, *Nature* **312**, 134 (1984).
12. M. McPherson *et al.*, *Sol. Phys.*, in press.
13. J. R. Kuhn, P. L. Lamy, H. Lin, S. Koutchmy, R. N. Smartt, in *Infrared Solar Physics* (International Astronomical Union Publ. 154, Paris, in press).
14. C. Lebecq, S. Koutchmy, G. Stellmacher, *Astron. Astrophys.* **152**, 157 (1985).
15. P. Lamy and S. Koutchmy, *Bull. Am. Astron. Soc.* **6**, 311 (1974).
16. A. W. Peterson, *Astrophys. J.* **146**, L37 (1967).
17. _____, *ibid.* **155**, 1009 (1969).
18. _____, *Bull. Am. Astron. Soc.* **3**, 500 (1971).
19. R. M. MacQueen, *Astrophys. J.* **154**, 1059 (1968).
20. T. Mukai and T. Yamamoto, *Publ. Astron. Soc. Jpn.* **31**, 585 (1979).
21. P. L. Lamy and J. M. Perrin, *Icarus* **76**, 100 (1988).
22. _____, *Astron. Astrophys.* **163**, 269 (1986).
23. K. Hodapp *et al.*, *Nature* **355**, 707 (1992).


24. This experiment was supported by the Laboratoire d'Astronomie Spatiale du CNRS, the Institut National des Sciences de l'Univers, the Canada-France-Hawaii Corporation, Michigan State University, National Solar Observatory/Sacramento Peak, and the National Science Foundation. The IR detector was developed at Rockwell under a collaborative agreement with the Astrophysical Research Consortium. Partial support for the array also comes from the University of Wyoming and Haverford College. We are grateful to D. Hoadley and N. Blair for help with the camera software and polarization analysis.

2 April 1992; accepted 5 June 1992


# Manipulation of the Wettability of Surfaces on the 0.1- to 1-Micrometer Scale Through Micromachining and Molecular Self-Assembly


Nicholas L. Abbott, John P. Folkers, George M. Whitesides*



**Micromachining allows the formation of micrometer-sized regions of bare gold on the surface of a gold film supporting a self-assembled monolayer (SAM) of alkanethiolate. A second SAM forms on the micromachined surfaces when the entire system—the remaining undisturbed gold-supported SAM and the micromachined features of bare gold—is exposed to a solution of dialkyl disulfide. By preparing an initial hydrophilic SAM from $HS(CH_2)_{15}COOH$, micromachining features into this SAM, and covering these features with a hydrophobic SAM formed from $[CH_3(CH_2)_{11}S]_2$, it is possible to construct micrometer-scale hydrophobic lines in a hydrophilic surface. These lines provide new structures with which to manipulate the shapes of liquid drops.**


A combination of micromachining (*1*) and molecular self-assembly provides the basis for a procedure that can be used to generate micrometer-scale patterns of contrasting surface properties. This procedure has three steps: (i) formation of an initial SAM of alkanethiolate on Au (*2*); (ii) generation of regions of bare Au in the SAM by micromachining; and (iii) formation of a second SAM on these micromachined regions. Because the two SAMs can have different compositions and physical properties and because the shapes of the micromachined features (*3*) can be controlled, this process controls the characteristics of a surface with micrometer resolution without the use of photolithography. We illustrate the capability of this type of microfabrication by forming patterns of SAMs of contrasting wettability on Au surfaces and by using these patterns to manipulate the shapes of drops of water.

The experimental procedure is summarized in Fig. 1. First, a hydrophilic SAM was formed by reaction of an Au film (*4*) with ω-mercaptohexadecanoic acid $[HS(CH_2)_{15}COOH]$ (*5*). The carboxylic acid group makes the surface hydrophilic, with wettability dependent on the pH of the water: the contact angle [measured under cyclooctane (*5*)] decreased from $\theta_a^{H_2O} = 30°$ (pH 5) to <5° (pH 10). Second, 0.1- to 1-μm features of bare Au were micromachined into the surface of the Au supporting the SAM. Either a surgical scalpel blade or the cut end of a carbon fiber was used as a tool (*6*). We used a 3 mN load on the tip of the scalpel to machine uniform grooves with macroscopic lengths (≥1 cm), widths of ~1 μm, and depths of ~0.05 μm (Fig. 2). The micromachined grooves were bordered by two lips of raised metal (~0.1 μm high and ~0.2 μm wide) formed by the plastic deformation of the Au during machining (*7*). Each lip presents an inclined surface to the edge of a spreading drop of liquid and influences the wetting behavior of the surface. In contrast, much smaller lips of metal bordered the ~0.1-μm-wide grooves that were formed with the tip of a carbon fiber (*8*). Third, a second, hydrophobic SAM was formed selectively on the bare Au features by immersion of the micromachined surface in a solution of $[CH_3(CH_2)_{11}S]_2$. We used a dialkyl disulfide in this step because the rate at which dialkyl disulfides replace surface thiolates in SAMs is ~1/100 of that of the corresponding alkanethiols and thus the dialkyl disulfides minimize the modification of the properties of the original hydrophilic SAM while forming the second hydrophobic SAM (*9*, *10*).

Features on the 0.1- to 1-μm scale having contrasting wettability can pin the edges of drops of water. The extent of this pinning was influenced by the type of SAM within the micromachined groove and by the shape of the groove (*11*). We have used grooves 0.1 to 1 μm wide having hydrophobic SAMs to manipulate the positions and the shapes of drops: several features that can be controlled are illustrated in Fig. 3.

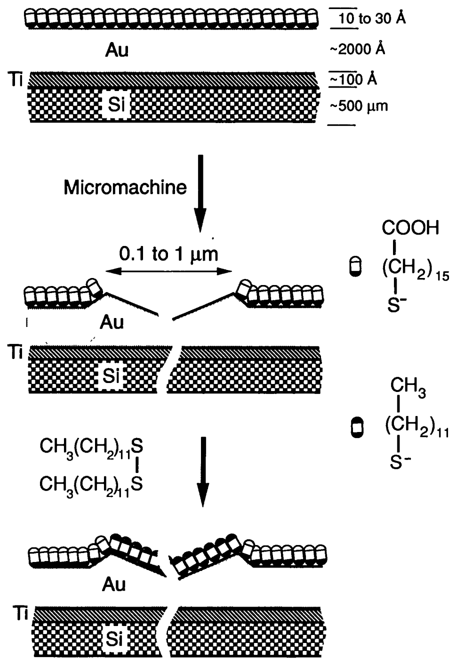


**Fig. 1.** Schematic illustration of the formation of 0.1- to 1-μm hydrophobic lines in a hydrophilic surface with micromachining and SAMs. We imply no asymmetry in the structure of the SAMs within the micromachined groove. Au, evaporated film of gold; Ti, evaporated film of titanium used to promote adhesion of the gold to the silicon wafer.


Department of Chemistry, Harvard University, Cambridge, MA 02138.

*To whom correspondence should be addressed.